Laser powder bed fusion of pure copper electrodes

Yahya Aghayar [a,*], Parisa Moazzen [a], Behrang Behboodi [a], Ayda Shahriari [a], Sajad Shakerin [a], Alan Lloyd [b], Mohsen Mohammadi [a]

[a] Marine Additive Manufacturing Centre of Excellence (MAMCE), University of New Brunswick, Fredericton, NB E3B5A1, Canada
[b] Department of Civil Engineering, University of New Brunswick, Fredericton, NB E3B 5A1, Canada

ABSTRACT

This study explores the fabrication and characterization of a pure copper electrode for an EDM equipment using laser powder bed fusion (LPBF) and comparing its performance with an original cast sample. The microstructural, mechanical, electrical, thermal, and corrosion characteristics of the samples were analyzed. The microstructure of the additively manufactured (AM) sample exhibited superior mechanical properties, with an 18 % increase in ultimate tensile strength and more than two times greater elongation in comparison with those of the cast sample. Moreover, the electrical and thermal conductivity coefficients of the AM sample were found to be consistent with industry standards as 5.52×10^7 S/m and 361 W/mK, respectively. Additionally, the potentiodynamic polarization corrosion test results of the AM sample further exhibited superior corrosion resistance in terms of the corrosion potential particularly in a 3.5 % NaCl environment. Advanced electron microscopy techniques were used to investigate the differences in the properties of the AM and cast samples and further shed light on the superior properties of the LPBF counterpart. Despite challenges in manufacturing pure copper components through LPBF, this study demonstrates the feasibility of producing a functional part that competes effectively with cast counterparts and excels in certain aspects.

1. Introduction

Pure copper finds extensive use in the electronics and aerospace industries due to its remarkable electrical and thermal conductivity properties. It boasts electrical conductivity coefficients of approximately 102 % of the International Annealed Copper Standard (IACS) and a thermal conductivity of approximately 400 W/mK. These exceptional properties render pure copper an ideal choice for various applications, particularly in the manufacturing of electromagnetic components and heat exchanger components [1–3]. This metal can be shaped into diverse forms and sizes due to its superior formability given the production process and its level of purity where elongations exceeding 124 % has been successfully attained [4]. The industry's demand for parts with smaller dimensions, reduced weight, and intricate geometries has led traditional manufacturing methods such as casting and forging to face new challenges. Consequently, researchers have recently turned their attention towards innovative fabrication technologies such as additive manufacturing (AM) to produce metallic parts with complicated shapes and geometries and competitive physical and mechanical properties [5–7].

Laser powder bed fusion (LPBF) has gained significant attention among other AM techniques owing to its distinctive capabilities and promising outcomes. One of the most important features of this method is the utilization of different laser sources (infrared, green, and blue) with various power levels (100 W to 1000 W) [8]. LPBF can be used to fuse different types of alloys and metals with various and specific physical characterization enabling processing alloys under high solidification rates. Additionally, LPBF can lead to produce components with superior surface quality and the manufacturing of parts with complex geometries [9]. In recent years, LPBF has been employed to produce parts from various alloys such as stainless steels [10], titanium [11], aluminum [12], and advanced high entropy alloys [13] to implement in a diverse group of applications. Recent studies have shown copper parts with favorable properties in terms of mechanical, thermal, and electrical characteristics can be produced through LPBF, although the fabrication of parts made from pure copper and its alloys using this method poses several challenges [14–17].

Working with pure copper powder presents a major challenge due to its high reflectivity when exposed to a laser beam. Copper, identified as the second most reflective material after gold in the selective laser

melting (SLM) method by Khan and Dickens [18], tends to reflect a significant amount of the laser beam. This reflection means that the desired energy does not effectively reach the copper powders, leading to issues like incomplete melting. To tackle this challenge, it is crucial to carefully choose the type of laser and adjust its power input appropriately [19,20]. Guan et al. [21] employed an infrared laser with a wavelength of 1060 nm and a power of 190 W to create a thin pure copper wall with a density of 82 %, while the reflectivity of an infrared laser against pure copper exceeds 95 % [22]. They indicated that altering the type of laser used in the LPBF process can impact the input energy emitted on the powder bed and the final properties of the fabricated parts.

In another study, Hori et al. [23] produced pure copper samples with a density of 99.1 % by utilizing a 200 W blue laser, whereas Gruber et al. [24] achieved densities exceeding 99.8 % by employing a green laser. Generally, the energy of a laser beam is directly proportional to its wavelength. Blue lasers, having shorter wavelengths (450–500 nm) than green lasers (500–550 nm), tend to possess higher energy per photon. This discrepancy arises from the fact that light with shorter wavelengths carry more energy, as described by $E = hc/\lambda$. In this context, the symbol 'E' represents the energy, 'h' denotes Planck's constant, 'c' signifies the speed of light, and λ is used to represent the wavelength of the laser beam [25]. Owing to their elevated energy per photon, blue lasers commonly exhibit greater power outputs compared to green lasers. Consequently, when a sample is produced using a blue laser, it imparts a higher amount of energy and power to the powder particles, resulting in reduced lack of fusion and increased density.

In addition to the numerous challenges involved in melting pure copper powders, such as the interaction between powder particles and the laser beam and the significant reflection, achieving a high density and high-quality samples necessitates the higher input energy. Recent findings illustrated that the utilization of insufficient energy input on pure copper powder can result in the partial melting of the powder, inadequate re-melting between the formed layers, and the emergence of various defects such as surface roughness, different types of porosities, cracks, and metal vaporization [15,26,27]. Several studies, see e.g., [20], have shown that increasing the laser power can increase the energy absorption capacity of copper particles, with the maximum absorption occurring between 350 and 550 W. On the other hand, increasing the laser power also results in an increase in the level of reflection. In this context, Gargalis et al. [26] suggested that, in addition to adjusting laser power, greater efficiency can be attained by altering the thickness of the powder layer. Therefore, selecting the appropriate laser type and laser power is crucial for applying the suitable energy input to powder particles. Furthermore, Silbernagel et al. [28] indicated that the alterations in the manufacturing orientation of pure copper specimens fabricated using LPBF can significantly impact their electrical resistivity. Specifically, horizontal, and inclined samples with a 45° angle exhibited the lowest electrical resistance [28].

One of the essential consumables used in the electrical discharge machining (EDM) equipment is copper electrodes [29]. These especially shaped electrodes with exceptional physical and mechanical properties can significantly enhance the operational efficiency of an EDM machine. To date, the prevailing focus of research has been on laboratory specimens, with limited attention directed towards the synthesis of practical copper samples possessing desired properties and high density—a matter of paramount importance. Given the pivotal role of manufacturing industrial and tool components, coupled with the acknowledged challenges associated with producing pure copper and copper alloys, this research endeavors to fabricate a pure copper component to employ in electrical discharge machining (EDM) equipment using laser powder bed fusion (LPBF) as an alternative to the conventional casting techniques. In pursuit of this objective, the initial phase of this study involves an extensive analysis of the microstructure and texture of two samples produced via LPBF and casting. Remarkably, discernible variations in microstructure have been noted at different heights within the AM specimen, warranting a comprehensive investigation. For the application of pure copper in EDM equipments, aside from its mechanical and corrosion-resistant properties, its thermal behavior and electrical conductivity assume paramount significance, and thus, these properties are subjected to rigorous scrutiny.

2. Materials and experiments

A pure copper electrode manufactured originally through a casting technique for the EDM industry was considered in this study. Fig. 1(a)–(c) show various views of the original cast component, which was utilized as the basis to design the component's geometry through CATIA software after 3D scanning and precise measuring of all dimensions, as shown in Fig. 1(d).

Table 1 presents the chemical composition of the sample, which was determined via spark atomic emission spectrometry in accordance with BS EN 15079:15 standard. Additionally, this table provides information on the electrical, thermal, and mechanical properties of the original cast sample.

The microstructure of both cast and AM samples were examined using a Zeta 3D imaging optical microscope according to ASTM E3:17 requirements for sample preparation. In addition, ASTM E407:15 was considered for etching the samples using a solution containing 5 gr $FeCl_3$, 16 ml HCl, and 60 ml ethanol.

Further advanced electron microscopy analysis was carried out using an FEI Scios 2 HiVac dual beam system equipped with multiple detectors. Scanning electron microscopy (SEM) was conducted using the dual beam instrument through an FEI NICol field emission gun (FEG) electron column. In addition, focused ion beam milling through an FEI High-throughput gallium ion column equipped with an FEI EasyLift EX Nano-Manipulator was employed to prepare the transmission electron microscopy (TEM) samples. The Scios 2 was additionally equipped with a Retractable directional backscatter (DBS) detector and a Retractable 30 keV scanning transmission electron microscopy (STEM) STEM 3 + detector to perform both analyses. The microscope was equipped with an Oxford energy dispersive spectroscopy (EDS) AZtecLive Advanced Microanalysis System with UltiMax 170 large area Analytical Silicon Drift Detector (up to 170 mm^2) along with the Oxford Aztec Energy software. In addition, a high resolution (1244 × 1024 pixels) Oxford Electron backscatter diffraction (EBSD) Symmetry® S3 detector (CMOS sensor technology) integrated with the AZtecHKL software was used for both EBSD and transmission Kikuchi diffraction (TKD) EBSD analyses. The X-ray diffraction (XRD) test also was performed on cast sample to identify the possible phases. The XRD pattern was obtained using a Bruker D8 DISCOVER equipment a 0.02° step size at 40 kV and 30 mA. The analysis of the X-ray measurements was conducted using DIFFRAC. Measurement Centre version 7.5 software and DIFFRAC.EVA version 6.0.

As shown in Fig. 2(a-c), the designed sample was additively manufactured with dimensions identical to the cast sample. The density of the part was measured using the Archimedes and mapping methods. This measurement was repeated five times, yielding a density of 98.4 % with an uncertainty of 0.53 % at a 95 % confidence level using a coverage factor of k = 2. The level of porosity and inconsistencies in the microstructure was analyzed using ImageJ software, with each measurement being repeated three times per image. The areas of interest in the part studied are shown in Fig. 2(d, e). The microstructure of various areas of the part produced by additive manufacturing was evaluated using different advanced electron microscopy techniques using the dual beam instrument. The resulting texture changes were analyzed via EBSD, while the fracture surface was examined using SEM. Moreover, to ensure that the AM part was free of any cracks or surface roughness, a non-destructive liquid penetrant test (PT) was performed according to ASTM E1417:21, see e.g., Fig. 2(f, g).

The mechanical properties of the samples were quantified using the Vickers method with a force of 10 gr using a ZHV30 low-load Vickers
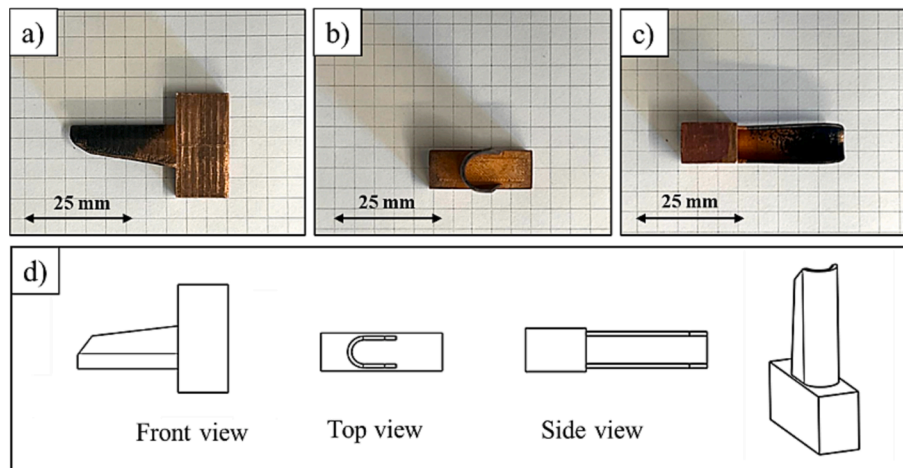
Fig. 1. The original (cast) copper electrode part used in the electrical discharge machining (EDM) equipment. a) Front view; b) Top view; c) Side view; and d) Technical drawing of the sample.

Table 1
Chemical composition, mechanical, electrical, and thermal properties of the original EDM electrode.

Properties	Chemical Composition (% wt.)				Yield Strength (0.02 %) (Mpa)	Tensile Strength (Mpa)	Elongation (%)	Hardness (HV)	Electrical Conductivity (S/m)	Thermal Conductivity (W/m.K)
	Cu	P	Te	S						
As-cast sample	99.2	0.09	0.69	0.02	197 ± 3	249 ± 4	9.0 ± 0.8	88 ± 1	$5.78 \times 10^7 \pm 0.07$	378 ± 4

The LPBF component was produced using a 99.9 % pure copper powders with no sign of oxygen with a mean diameter size of 30–45 μm through an EOS M290 additive machine. The process parameters as illustrated in Table 2 were used during the LPBF process.

Table 2
Laser powder bed fusion (LBPF) process parameters used to manufacture the copper EDM electrode.

Process Parameters	Constant value
Machine model	EOS M290
Laser type	Infrared
Laser power	380 W
Hatch space	0.14 mm
Layer thickness	30 μm
Scan speed	300 mm/s
Inert gas	Argon
Substrate material	316L stainless steel
Energy input (p = power, v = scan speed, h = hatch space, t = layer thickness)[30]	$E = \dfrac{P}{V \times h \times t} = 301$ (J/mm³)

hardness equipment following the guidelines outlined in ASTM E92:17. The uniaxial tensile tests were conducted under the requirements of ASTM E8:21 utilizing an INSTRON-5985 universal testing machine, incorporating a 25 mm extensometer and a strain rate of 10^{-3} s^{-1}. The dimensions of the miniature uniaxial tensile specimens are shown in Fig. 2(d), which were machined out of the LPBF sample as closest possible to ASTM E8:21 standard. The tests were repeated three time to make sure about the repeatability and a typical stress–strain curve was subsequently documented. The yield strength value was calculated using the 0.2 % offset method. To accurately assess the tensile properties of the additively manufactured part, digital image correlation (DIC) method was employed for the uniaxial tensile test procedure. DIC was employed in conjunction with an ARAMIS 6.1 system to effectively visualize the variations in the strain field and the eventual failure of the test specimens. The samples were sprayed with black and white paint (fine speckle pattern) to detect their precise movement being able to accurately identify their displacement and the final strain field.

In accordance with the part's intended application environment, the

potentiodynamic polarization tests were conducted to the surface of the cast and the LPBF copper samples in two different environments, namely distilled water, and a 3.5 wt% NaCl solution, which can be representative for the EDM application. To measure the electrical resistance, three samples with dimensions of $1 \times 10 \times 30$ mm³ were prepared, and the 4-point technique was used according to ASTM B193-02. Furthermore, the thermal conductivity of the samples was calculated by measuring the electrical conductivity using the Wiedemann-Franz equation [31].

3. Results and discussion

3.1. Microstructural characterization

3.1.1. Cast sample

The microstructure of the cast sample, observed through optical microscopy (OM) at two different magnifications, is depicted in Fig. 3(a and b). It is evident that the microstructure comprises of grains containing twins within the Cu matrix, along with semispherical particles that are uniformly distributed throughout the microstructure. To perform an extensive investigation of the particles and their chemical composition, SEM imaging (Fig. 3(c)) and chemical composition analysis (EDS) of the particles and the matrix (Fig. 3(d–f)) are analyzed. The XRD shown in Fig. 3(g) also depicts the presence of Cu_2Te in this alloy. According to the presence of twins and the specific shape of grains, it can be presumed that the microstructure of the cast component is the result of a thermomechanical operation resulted in the distribution of particles containing Te. It is well-known that the annealing twins form after severe plastic deformation and annealing processes. In addition to the good electrical and thermal properties of this alloy, the presence of tellurium-containing particles will also lead to a significant improvement in machining properties. This type of microstructure and precipitations has also been reported in other studies on Cu alloys [32–34].

Fig. 4(a) and 4(b) illustrate the sample preparation using FIB milling technique to extract a TEM lamella for STEM investigation and a cross-
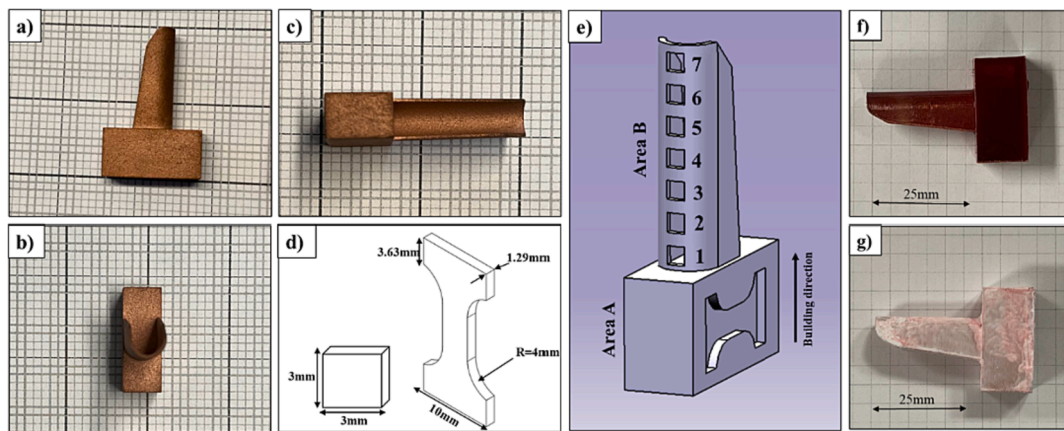
Fig. 2. Additively manufactured part. a) Front view; b) Top view; c) Side view; d) The prepared samples for the uniaxial tensile test and microstructure analysis were in the shape of rectangular bars with dimensions of $3 \times 1 \times 3$ mm^3. The uniaxial tensile test specimens were prepared according to ASTM E8:21; e) Schematic of the locations of the test samples used for the uniaxial tensile tests and microstructural evaluation from part A and B, respectively; f) The sample under the PT test (penetrating stage); and g) The sample after the PT test (final stage).
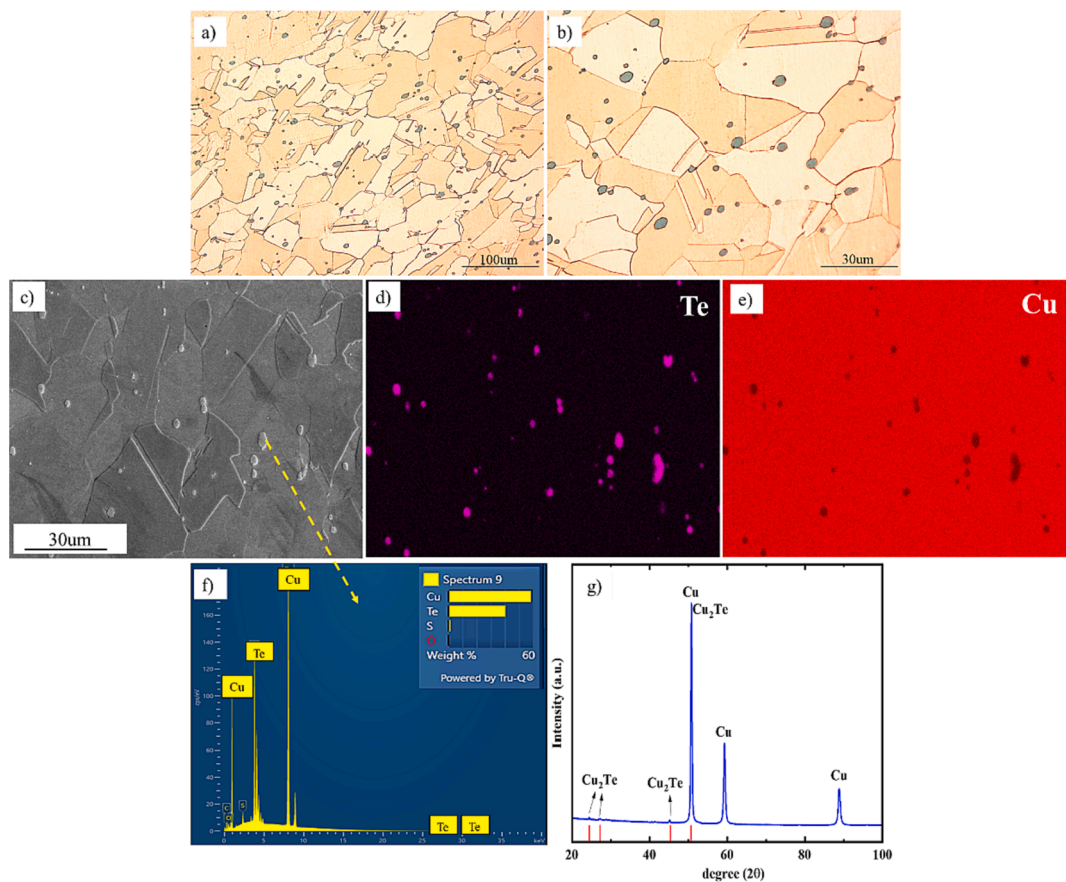

Fig. 3. Characterization of the original EDM electrode cast part microstructure. a) low magnification; and b) high magnification optical microscope image of the cast part microstructure; indicating Cu grains including thermomechanical twins and distributed Te-precipitations; c-f) EDS maps of the matrix and the particles distributed in the microstructure and g) XRD pattern of the cast sample.

sectional view of the microstructure of this sample, respectively. Twins with thicknesses equal or less than 2 μm and precipitations with sizes ranging between 1 and 5 μm was observed. EDS analysis under STEM mode confirmed the presence of a small percentage of the (Fig. 4(d)) in the Cu matrix (Fig. 4(c)), resulting in the formation of copper telluride (Cu$_2$Te) that have a significant impact on the machinability and mechanical properties of the alloy and improve its abrasive performance. Cu$_2$Te is a semiconductor material with a narrow bandgap, typically

around 0.5–0.6 eV. This bandgap makes it suitable for applications in thermoelectric devices, where it can efficiently convert heat into electricity. Moreover, Cu$_2$Te exhibits good electrical conductivity, which is advantageous for electronic and optoelectronic applications. The effective parameters in reducing the electrical conductivity of the commercial alloy compared to pure copper can be attributed to the number of dislocations in the microstructure, the amount of grain boundaries, and the electrical resistance of Cu$_2$Te. The electrical resistance of Cu$_2$Te is
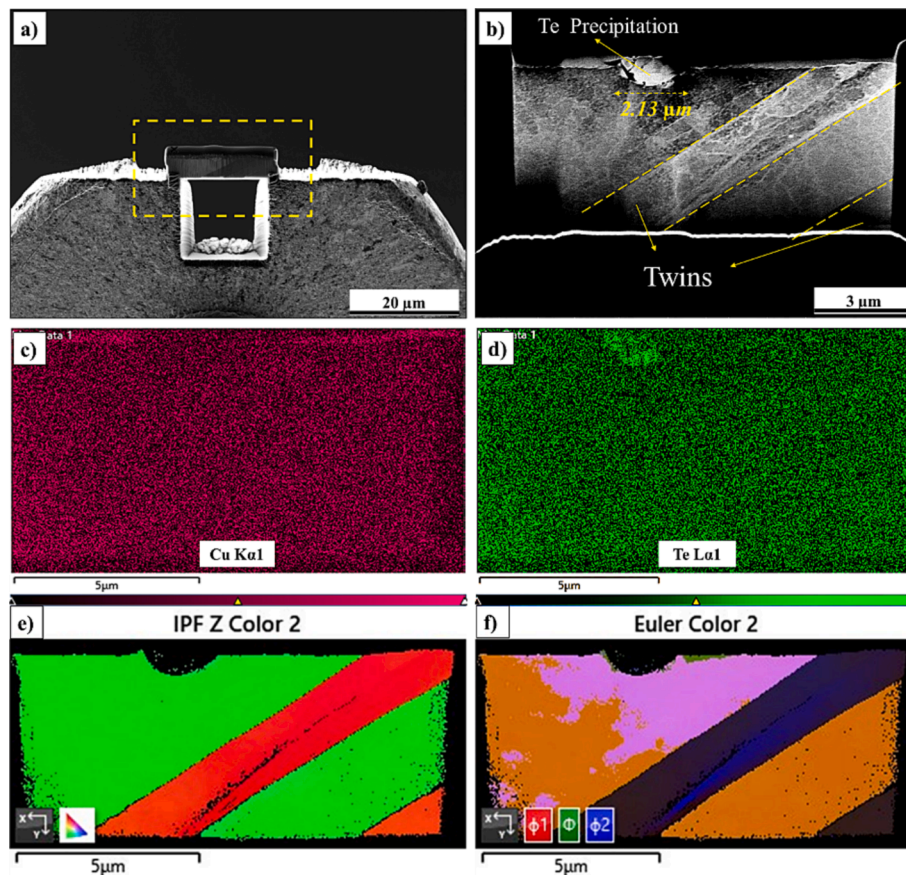
Fig. 4. Scanning transmission electron microscopy (STEM) analysis of the cast sample. a) FIB lamella; b) STEM mode image; c) EDS Map analysis of Cu matrix; d) Map analysis indicating the presence of Te- intermetallic precipitations; e) IPF map (The red regions are the annealing twins within the green grains); and f) Euler image of the FIB lamella conducted by the EBSD detector (TKD-EBSD). (For interpretation of the references to colour in this figure legend, the reader is referred to the web version of this article.)

approximately 1.6×10^{-5} Ωm. Along with other factors contributing to electrical interference, these elements have brought the electrical conductivity of the alloy to about 5.57×10^7 (S/m). However, the appropriate electrical conductivity of Cu_2Te has not led to a significant reduction in the electrical conductivity of the alloy compared to pure copper. These particles are dispersed in the microstructure as a semiconductor with excellent thermoelectric properties. This dispersion has not caused a significant drop in the electrical and thermal properties of the original pure copper and has maintained the electrical and thermal properties of the alloy in significant amounts [33,35,36].

The inverse pole figure (IPF) and the EBSD Euler angles ϕ_1, Φ and ϕ_2 maps of the cast sample are shown in Fig. 4(e) and 4(f) (TEM lamella (TKD-EBSD)). IPF images are effectively revealed distinct crystalline orientations within the Cu matrix (1 0 1) and the twins (0 0 1) [37]. Multiple theories have been proposed for the formation of the twins, describing three primary mechanisms. The initial theory suggests that crystals with an inherent twin relationship collide during growth, leading to the subsequent formation of twins [38]. The second theory posits that twins arise when a layer of atoms becomes misplaced on the (1 1 1) plane due to the presence of low stacking fault energy [39]. Lastly, the third theory hypothesizes that grain boundaries with higher energy undergo a transformation into twin boundaries, while lower energy grain boundaries remain unaffected. Consequently, the continuous occurrence of annealing twins during recrystallization signifies an ongoing evolution, and the existing evidence fails to distinguish definitively between these theories [40].

3.1.2. LPBF samples
To examine the microstructural aspects of the LPBF sample, all areas

of the part were thoroughly studied. The microstructure of the rectangular cube part of the piece (Area A in Fig. 2(e)) was evaluated using OM and SEM, as depicted in Fig. 5. There are some discontinuities, which prevent achieving a homogeneous microstructure, resulting in a density that is below 100 % (Fig. 5(a)). These defects occur due to inadequate energy transfer to the powders during the printing process, resulting in partial melting or non-melting of the powders. This leads to failure to achieve complete bonding between adjacent areas. Increasing the energy input by raising the laser power or lowering the laser scanning speed can provide complete melting of the powders and higher densities; however, such methods may result in equipment damage due to high reflection of Cu powders, or an increase in grain size. This impacts the mechanical properties and fatigue behavior of printed parts [41,42]. The percentage of these discontinuities was measured to 1.14 %± 0.07using the ImageJ software (Fig. 5(b)).

Accordingly, the existing defects can be classified into two distinct categories based on their shape. The first category encompasses defects with larger dimensions and hole shapes. As observed in Fig. 5(c), unmelted powders can be seen in these defects, appearing as black areas in the microstructure. The non-melting of these powders results in a gap (lack of fusion) between two completely continuous areas and has a considerable impact on the reduction of density. Lack of fusion (LOF) defects are a significant issue encountered in samples manufactured with low densities. These defects can be attributed to various factors, including insufficient energy input, improper scanning technique, or inadequate preparation of the powder bed. Insufficient melting or bonding of neighboring layers is the primary cause of LOF defects. The high thermal gradient surrounding LOF defects contributes to an increased presence of dislocations and defects in the microstructure
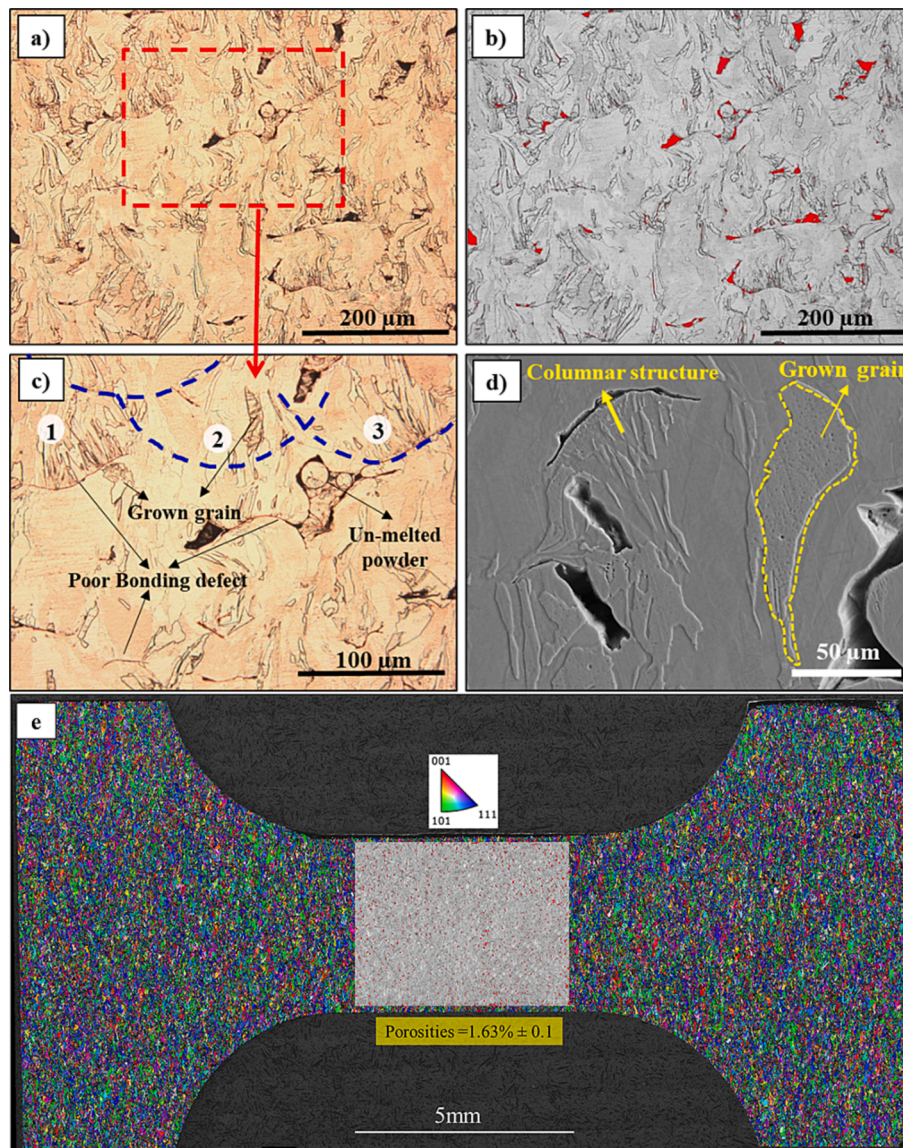
Fig. 5. Microstructural analysis of pure Cu additively manufactured part. a) OM images from the rectangular area of the part that shows different kind of defects and discontinue; b) Porosity area calculated by ImageJ software; c) different kind of melt pools formed in around various situation in terms of solidification rate and un-melted powders stacked inside of the porosities; d) SEM image of the melt pools and grain growth inside an intact melt pool; and e) The IPF map of the tensile sample along with the percentage of the porosities in gage length.

further promoting the formation of smaller grains [43]. The second category of defects, which resemble cracks, occurs precisely at the border of the melt-pools, and are formed due to poor bonding between the melt pools. It is worth noting that the microstructure around these defects is different from other regions (Fig. 5(c)).

It is evident that three distinct melt-pools have formed in the sample, each with their own unique features, see Fig. 5(c). Notably, melt pool number 1, which is surrounded by a poor bonding defect, has developed oriented columnar microstructures towards the center. Moreover, this defect may contain trapped gases, which serve as a coolant and cause a temperature gradient leading to the formation of a columnar solidification structure [44–46]. It can be seen in melt pool number 3 that half is intact, and the other half has a poor bonding defect. As long as the bonding is fully formed in intact region, no traces of the columnar structure resulting from rapid solidification can be seen, while a finer microstructure can be seen around the defective region. Furthermore, it can be observed that when melt-pools are formed one after the other without creating any defects between them (as in melt-pool number 2), the thermal gradient occurs at a lower rate. As a result, each melt pool

transfers part of its heat to the previous one, leading to microstructure homogenization, grain growth, and uniformity. In fact, the heat present in an intact melt pool is transferred at a lower rate compared to melt pool that leads to a porosity that causes the grain growth which is shown in Fig. 5(d). To more precise investigation a large IPF map was carried out from the whole tensile sample to measure the porosity percentage of this area (Fig. 5(e)). Due to this image and the measurement, it has been seen that the amount of the porosities in all over the tensile sample is 1.63 ± 0.1 % which is near to the pervious amount that measured in area A.

Owing to the geometrical modifications and thickness alterations in the upper segment (area B) of the component, a comprehensive investigation of the microstructure in the building direction along the height was conducted at the designated positions, as illustrated in Fig. 2(e). Specifically, the microstructural characteristics and porosity content were analyzed from the bottom to the top using optical microscopy and EBSD techniques. The microstructure of this area was found to be distinct from that of area A, as evident in Fig. 6(a), primarily due to the variations in the porosity percentage. The minimum amount of porosity
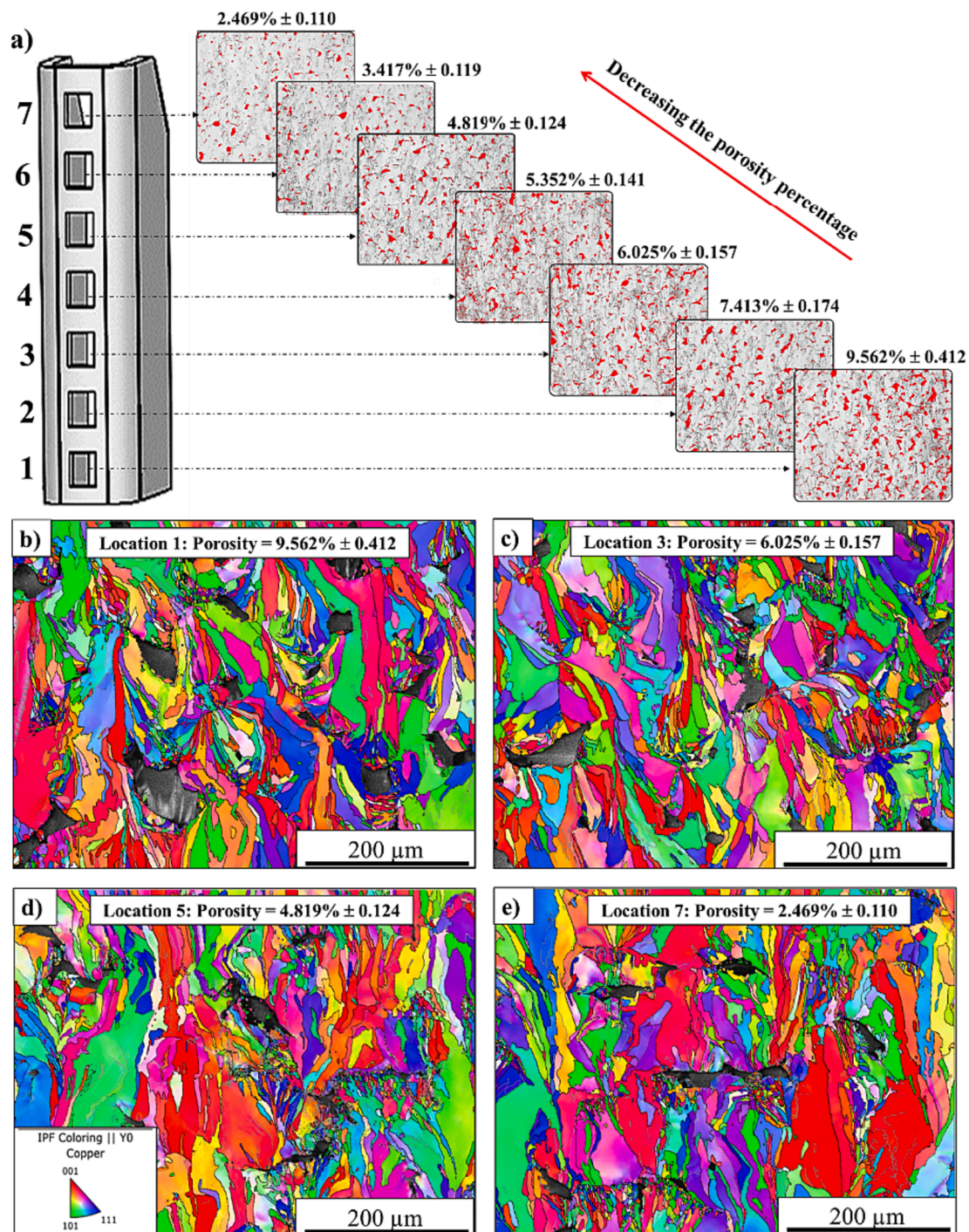
Fig. 6. Microstructure and porosity evolution along the height in the area B. a) Percentage of the porosities from the bottom to the up using ImageJ that shows the reduction of the porosities in building direction; b) IPF map of location 1 with maximum amount of porosities, c) location 3, d) location 5, and e) location 7 (The highest location contains the lowest percentage of porosity).

was detected in the uppermost region at a rate of approximately 2.5 % (location 7), which was higher than the porosity content in area A. It is well-known that one of the most critical geometrical factors impacting the microstructure and ultimate properties of LPBF produced components is thickness modification. Decreasing the thickness of a part leads to an increase in the cooling rate of successive layers, resulting in incomplete melting of the powders or their partial melting, which in turn increases the porosity percentage [47,48].

As depicted in Fig. 6, the percentage of porosity declines by approximately 7 % from location 1 to location 7 (bottom to top) of Area

B. All porosity values from location 1 to 7 are listed in the second column of Table 3. Accordingly, an upward trend in height corresponds to a notable reduction in porosities, accompanied by a subtle increment in the average grain size. During the layer-by-layer deposition process, a thermal profile is generated between adjacent layers, whereby the heat from the lower layer influences the cooling and solidification of the upper layer. As the height of the component increases due to the accumulation of layers, the heat from previous layers is transferred to the upper layers. This contrasts with the initial layers, where a considerable proportion of the incoming heat is transmitted to the substrate or lower

Table 3
Porosities, grain size values, and Vickers hardness estimates of the LPBF pure copper part along the height in the upper area (Area B).

Location	Porosity %	Average Grain size (um)	Hardness (HV)
1	9.562 % ± 0.412	7.9 ± 0.07	93 ± 2
2	7.413 % ± 0.174	8.1 ± 0.07	91 ± 1
3	6.025 % ± 0.157	8.1 ± 0.06	90 ± 2
4	5.352 % ± 0.140	8.4 ± 0.08	88 ± 2
5	4.819 % ± 0.124	8.5 ± 0.07	86 ± 1
6	3.417 % ±0.119	8.5 ± 0.08	86 ± 2
7	2.469 % ± 0.110	8.6 ± 0.09	84 ± 2

sections. The heat stored in the lower layers promotes superior melting of the powders in the upper layers, ultimately leading to a reduction in the porosity percentage and an increase in density in these regions [49,50].

The IPF maps (Fig. 6(b–e)) illustrate the variations in the microstructure and grain size along the height of the component from location 1 to 7. The average grain size undergoes alterations with an increase in height, ranging from approximately 7.9 μm in location 1 (Fig. 6(b)) to 8.6 μm in location 7 (Fig. 6(e)). The presence of pores ultimately changes the microstructure and specifically grain size of the component moving from bottom to top by changing the temperature field. The

microstructural changes were minimal around smaller holes, whereas significant changes in terms of size and morphology were observed around larger porosities. Specifically, larger holes acted as thermal insulators, preventing the transfer of heat from the melt pools to one another, this led to an elevated cooling rate, resulting in the formation of finer grains [51].

Moreover, the hardness values were measured through the height of the sample in Area B and they are listed in column 4 of Table 3. The hardness of the lower regions, despite having a higher percentage of porosity, was almost 9 % higher than that of the upper regions due to the presence of finer grains. The changes in grain size manifested a variation in the hardness values at different locations of the copper component as per the Hall-Patch relationship [52].

3.2. Texture analysis

Fig. 7(a, b) presents IPF maps for both the original cast and LPBF samples. It is obvious that the LPBF sample exhibits a notably smaller equivalent grain size in comparison to the cast sample. Furthermore, a stark divergence in grain orientations is evident between the two samples, signifying pronounced differences in their respective textures. The texture refers to the alignment of crystalline orientations within a polycrystalline material exerting a profound influence on numerous
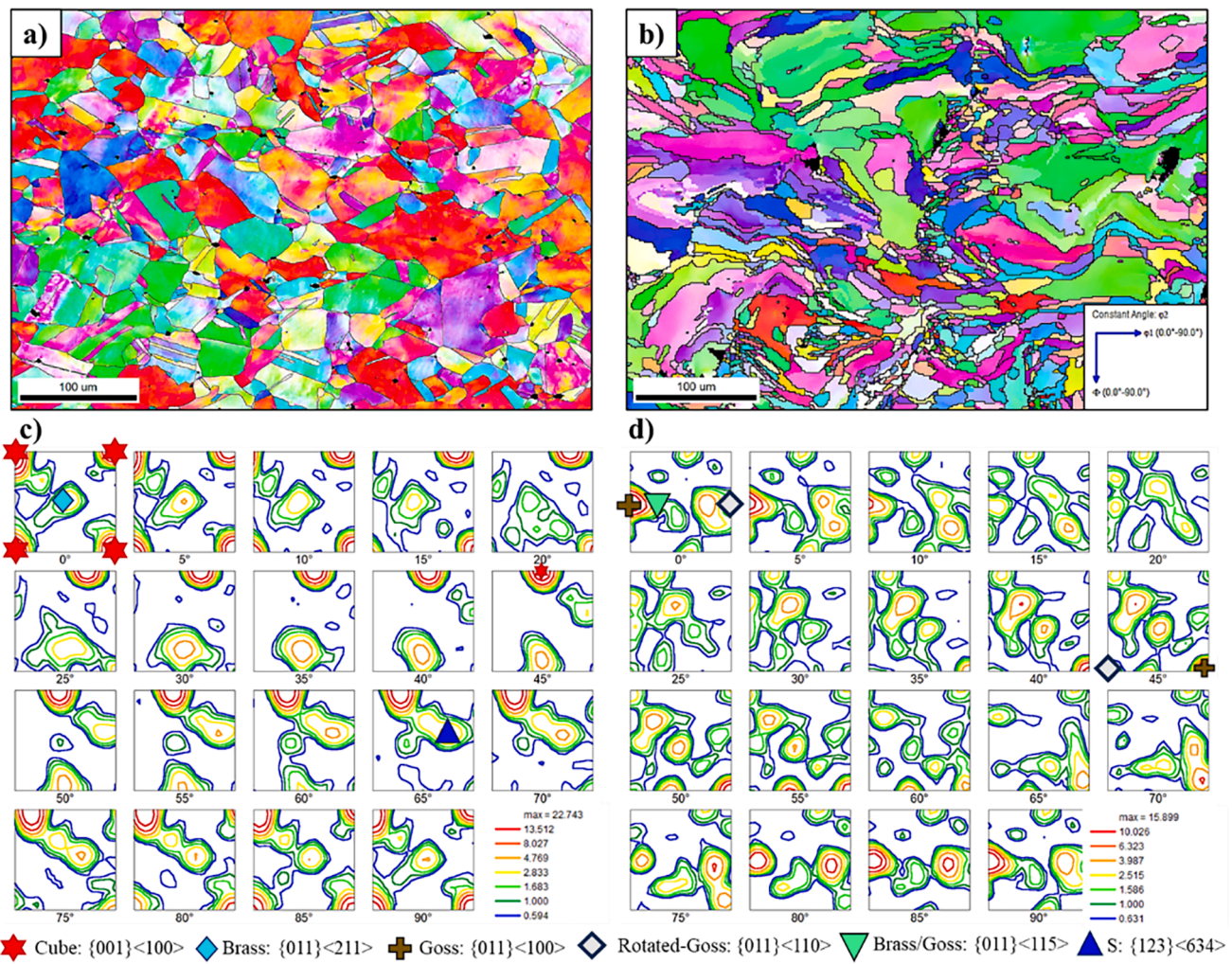
Fig. 7. IPF maps of a) the cast sample showing copper grains with different orientation and black holes which identify the Te precipitates, and b) LPBF pure Cu sample; Orientation distribution functions (ODFs) sections of c) the cast sample, and d) Printed pure Cu. The fabrication of Cu using the LPBF method results in a significant change in grain orientation and the presence of different textured components, particularly with a Goss {011} ⟨100⟩, Rotated-Goss {011} ⟨100⟩, and Brass/Goss {011} ⟨115⟩ orientations.

mechanical and physical characteristics. To investigate the texture evolution of both cast and LPBF samples, φ_2 constant sections of orientation distribution functions (ODF) are presented in Fig. 7(c, d). The important texture components are effectively demonstrated at three distinct φ_2 constant sections: 0°, 45°, and 60°.

It can be seen that Cube {001} ⟨100⟩, Brass {011} ⟨112⟩ and S {123} ⟨634⟩ texture components are revealed in ODF sections of cast sample indicating a substantial presence of twin boundaries within the microstructure. The Cube texture in copper is commonly attained via specialized production techniques, such as cold rolling or recrystallization during annealing. As a result of these processes, the crystal grains within the material exhibit a favored alignment, characterized by {001} planes. The emergence of a pronounced Brass texture component is typical in low-stacking fault energy (low SFE) materials primarily induced by intensive cold rolling and annealing processes [53–55].

The ODF sections of the LPBF Cu sample reveals a robust Goss-type texture component {011} ⟨100⟩ with significant intensity peaks in proximity to the Rotated Goss {011} ⟨100⟩ and Brass/Goss {011} ⟨115⟩ texture components along the ⟨110⟩//ND fiber direction. It has been reported that crystal planes with high-density close-packing exhibit superior resistance to chemical attacks and improved passivation

and repassivation characteristics [56]. In this current study, the LPBF Cu displays a high-packing density of crystal faces of the {110} type in the FCC structure.

3.3. Mechanical properties

To investigate the mechanical properties of the printed sample and compare them with the initial cast counterpart, three uniaxial tensile tests were performed using DIC. The engineering stress–strain curve of the LPBF sample and the corresponding DIC results are illustrated in Fig. 8 (a). The DIC results indicated a uniform elastic deformation in the sample that persisted until reaching the yield point at 205 ± 3 MPa (point 2). Subsequently, plastic deformation occurred and continued with greater intensity, particularly in the middle of the gauge (point 3 to 10). After attaining the ultimate tensile strength of 294 ± 3 MPa (point 10), subsequent loading and initial necking (point 11) were observed in the sample. Eventually, the sample develops the first signs of failure at point 11; this type of failure were also observed by Ghoncheh et al. [57] in an Al alloy produced via LPBF. This process of hole formation and crack propagation (post-necking) eventually led to the fracture of the sample (point 14). Remarkably, the sample did not fail before reaching
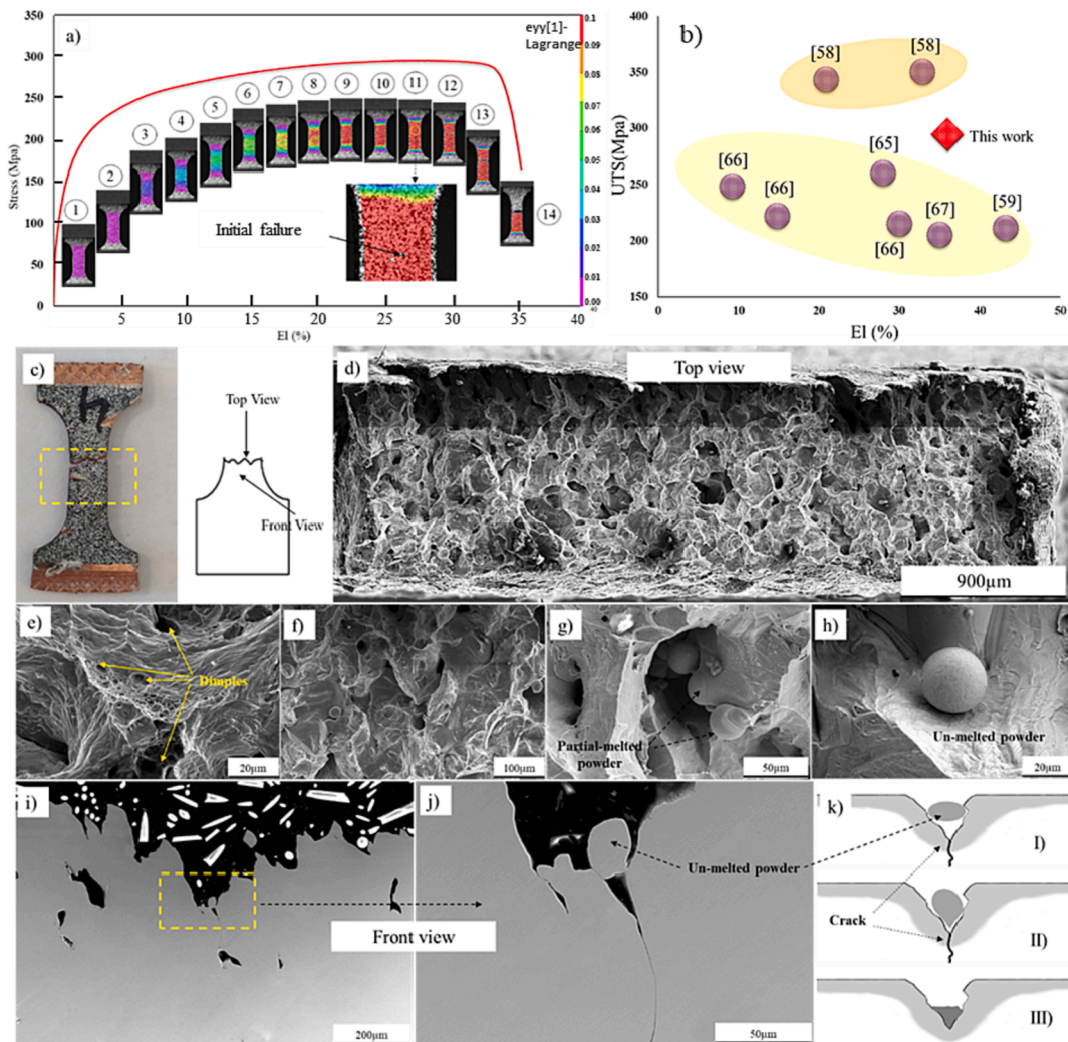
Fig. 8. Results of uniaxial tensile test of additively manufactured pure Copper sample. a) Stress–strain curve accompanied by DIC results; b) A comparison between uniaxial tensile properties presented in this work and the literature on pure copper produced by LPBF [58,59,65–67]; c) Uniaxial tensile test specimen after fracture; d) Fracture surface identification carried out by SEM (top view); e) Presence of dimples on the fracture surface, which proves ductile fracture; f) High magnification of fracture surface; g) Partially melted powders on the fracture surface; h) Un-melted powder located on the fracture surface; i) Low magnification front view of the fracture surface; j) High magnification front view of the fracture surface; k) A schematic of how porosities could be filled with and preventing of crack formation by melting the un-melted powders.

the ultimate tensile strength (point 10) at 294 ± 3 MPa and elongation to 34 % ± 3, despite the presence of over 1 % porosity in this section of the uniaxial tensile specimen. However, it is worth noting that the LPBF sample in this study showed a higher ultimate tensile strength compared to the cast sample, which had a strength of 227 ± 3 MPa. This indicates that the LPBF process can ultimately improve the mechanical properties of pure copper despite not being fully dense (~98 % instead of 99.9 %).

Fig. 8(b) presents a comparison between the mechanical properties of LPBF pure copper in this work and other samples produced by LPBF based on ultimate tensile strength and elongation found in the literature. Two family of data can be collected from the literature, one with higher ultimate tensile strength (packet A) and one with superior elongation (packet B). Qu et al. [58] used a high precision LPBF technique that generated an anisotropic properties and reported superior tensile properties. Moreover, Jadhav et al. [59] presented samples with the highest elongation, which is produced by LPBF machine equipped with an infrared fiber laser with wave length of 1080 nm. It is noteworthy to mention that the result from this study yielded a sample that has the benefit from both packets, where a combination of optimum tensile properties and elongation was achieved.

Additionally, the fracture surface of the uniaxial tensile specimen underwent evaluation via SEM for fractography. Fig. 8(c) illustrates the fractured sample, and the areas evaluate including the top and the side views. Fig. 8(d) shows a large scan composite image consists of many SEM images of the fracture surface from the top view of the sample. The presence of many dimples on almost the entire fracture surface confirms the ductile fracture and extended elongation that was observed in the uniaxial tensile tests. Fig. 8(e) shows a higher magnification of the fracture surface highlighting the dimples. They are in different dimensions and various depths indicating a ductile fracture in the sample. The presence of a greater number and deeper dimples in a material signifies its enhanced resistance to fracture, thereby augmenting its toughness [60,61].

Fig. 8(f) confirms the presence of other components including metal particles on the fracture surface that can cause the ultimate failure. At higher magnification of the top view fracture surface, both partially melted powders (Fig. 8(g)) and even un-melted pure copper particles (Fig. 8(h)). Zhong et al. [62] and Chen et al. [63] also reported similar results, which is mainly related to the LPBF processing of pure copper. The deep holes around the un-melted powders suggest that these areas are the origin of porosity formation and cracks that lead to failure in the sample. The vacancies around the un-melted powders create stress concentration sites during the uniaxial tensile test procedure, causing the porosity formation, and ultimately affecting the tensile properties of the sample [64]. The front view of the fracture surface can clearly prove this phenomenon as shown in Fig. 8(i) and (j), where a crack propagated just underneath an un-melted powder leading to failure under uniaxial tension. It can be concluded that, complete melting of all copper powder particles could thoroughly prevent the formation of such cracks during the uniaxial tensile test procedure by filling the empty spaces and lowering the stress concentration factor. Therefore, applying enough heat to melt the powder could significantly enhance the tensile properties of the sample [50,51]. Fig. 8(k) presents a schematic of the hypothesis that was presented, where un-melted powder particles could stop the growth of cracks and restrict their propagation by filling the gaps.

3.4. Electrical and thermal properties

To determine the electrical conductivity, σ, of the LPBF and cast samples, the following equation was utilized:

$$\sigma = \frac{l}{A \times R} \tag{1}$$

where R represents electrical resistance, A denotes the sample's area,

and *l* represents the length of the sample [68]. Initially, the electrical resistance of each sample was measured and then the electrical conductivity was subsequently calculated. Furthermore, the Wiedemann-Franz equation [31,59] was employed to determine the coefficient of thermal conductivity, k, of both samples and it is written as follows:

$$k = \sigma \times K \times L \tag{2}$$

where K represents the temperature in Kelvin, L is the proportionality constant of 2.2×10^{-8} (WΩK^{-2}), and σ is the electrical conductivity coefficient. The electrical conductivity coefficient of the LPBF sample was approximately 5.52 S/m, which was 0.26 S/m lower than that of the original cast sample, i.e., 5.78 S/m. Fig. 9(a) shows a comparison between the electrical conductivity values studied in this work and the published literature on LPBF pure copper. Based on the comparison presented in Fig. 9(a), the LPBF sample performs comparatively better than other samples additively processed in previous studies, particularly those that did not go through heat treatment procedures. One possible reason for this phenomenon can be attributed to the impact of heat treatment on the grain size and the quantity of grain boundaries. According to the results presented by Bishara et al. [69], there is a direct correlation between larger grain sizes and a reduction in grain boundaries, resulting in a subsequent decrease in electrical conductivity.

The thermal conductivity coefficient of the LPBF sample was calculated as ~ 361 W/mK. The cast counterpart showed slightly higher conductivity coefficient of ~ 378 W/mK, which was 4.5 % higher than that of the LPBF sample. Fig. 9(b) illustrates a comparison between the thermal conductivity coefficients calculated in this study in comparison with the available published literature. Upon comparing the results to other available data, it is evident that the thermal conduction coefficient of the LPBF sample lies within a satisfactory range for similar applications. The outcomes of prior research in this field have demonstrated that conducting heat treatment and reducing porosity can lead to an increase in the thermal and electrical conductivities of the AM samples [70]. Therefore, it can be inferred that the primary reason for the observed difference in the levels of thermal and electrical conductivity between the printed and cast samples is due to the presence of porosities and discontinuities in the microstructure [28].

3.5. Potentiodynamic polarization measurements

Due to the operating conditions of the electrode additively manufactured in this study, it was crucial to conduct a corrosion study in an aqueous environment. To this end, corrosion tests were executed using the potentiodynamic polarization method was applied in both distilled water and a 3.5 wt% NaCl solution. Fig. 10(a) and (b) depict the potentiodynamic polarization plots of both the additively manufactured samples (A1 and A2) and cast samples (C1 and C2) in these two environments. Furthermore, the SEM micrographs of the surface of the LPBF and cast specimens after potentiodynamic polarizations tests at 3.5 wt% NaCl solution are displayed in Fig. 10(c)-(f).

It is evident from Fig. 10(a) that there is no significant contrast in the corrosion behavior of the two samples in the distilled water environment. However, it can be observed that even in this setting, the cast sample experiences a slightly higher intensity of corrosion current and corrosion rate in comparison with its LPBF counterpart. Conversely, in the salty environment, the disparity between the two samples is more prominent (Fig. 10(b)). The variations of the corrosion current density (I$_{corr}$), corrosion potential (E$_{corr}$) accompanied with the anticipated corrosion rates, as well as the anodic and cathodic Tafel slopes denoted as βA and βC, respectively, have been included in Table 4. The corrosion parameters shown in Table 4 are calculated by fitting the Tafel equation to the linear sections of the anodic and cathodic branches of the Stern diagram obtained from the potentiodynamic polarization tests [71]. The value of χ^2 (chi-squared) presented in the Table 4 is in the order of magnitude of 10^{-6} to 10^{-10}, indicating a fair fitness between the
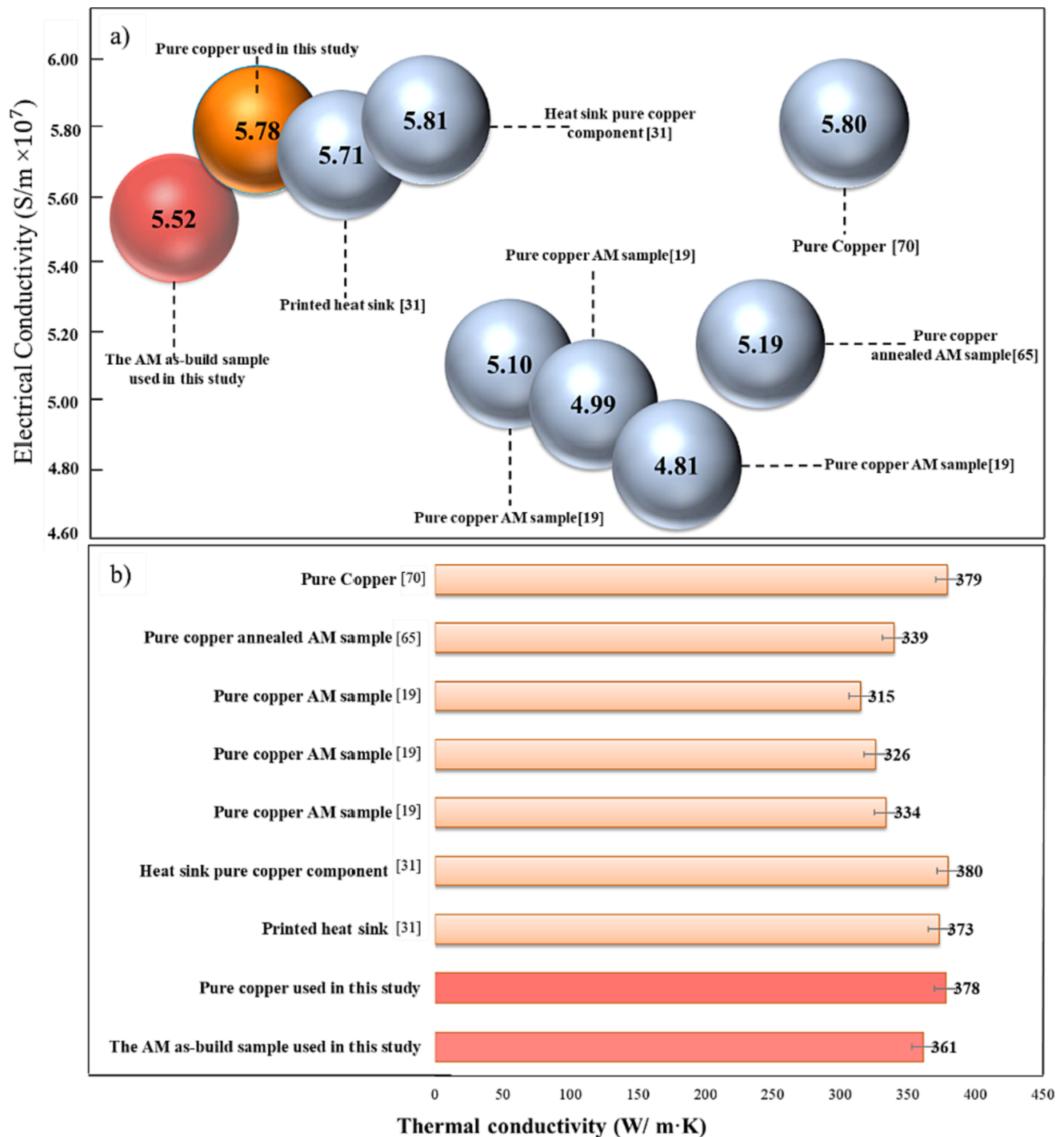
Fig. 9. A comparison between this work and other research on pure copper samples [19,31,65,70] in terms of a) electrical conductivity and b) thermal conductivity that show in both cases additively manufactured parts has fairly similar properties compared to the original one despite of the presence of porosity and discontinuities in the microstructure of the LPBF sample.

experimental values and the calculated values using Tafel equation as follows:

$$\eta_A = \beta_A \, Log\left(\frac{i_A}{i_o}\right) \qquad (3)$$

$$\eta_C = \beta_C \, Log\left(\frac{i_C}{i_o}\right) \qquad (4)$$

where ηA and ηC are over potential anodic and cathodic branches of the electrochemical reactions, respectively, βA and βC are the kinetic

parameters related to the Tafel equations named as anodic and cathodic Tafel slopes, respectively.

As depicted in Table 4, the potentiodynamic polarization plot of the LPBF sample (A2) exhibited a shift towards the top and left when compared to that of the as-cast sample (C2). This shift led to a decrease in the corrosion current density of the A2 sample indicating a lower corrosion rate (approximately 6.942×10^{-3} (mpy)) in comparison with the C2 sample (548.5×10^{-3} (mpy)) in the 3.5 wt% NaCl solution. Furthermore, the corrosion parameters provided in Table 4 demonstrated that the corrosion current (I_{corr}) values for both the LPBF and as-
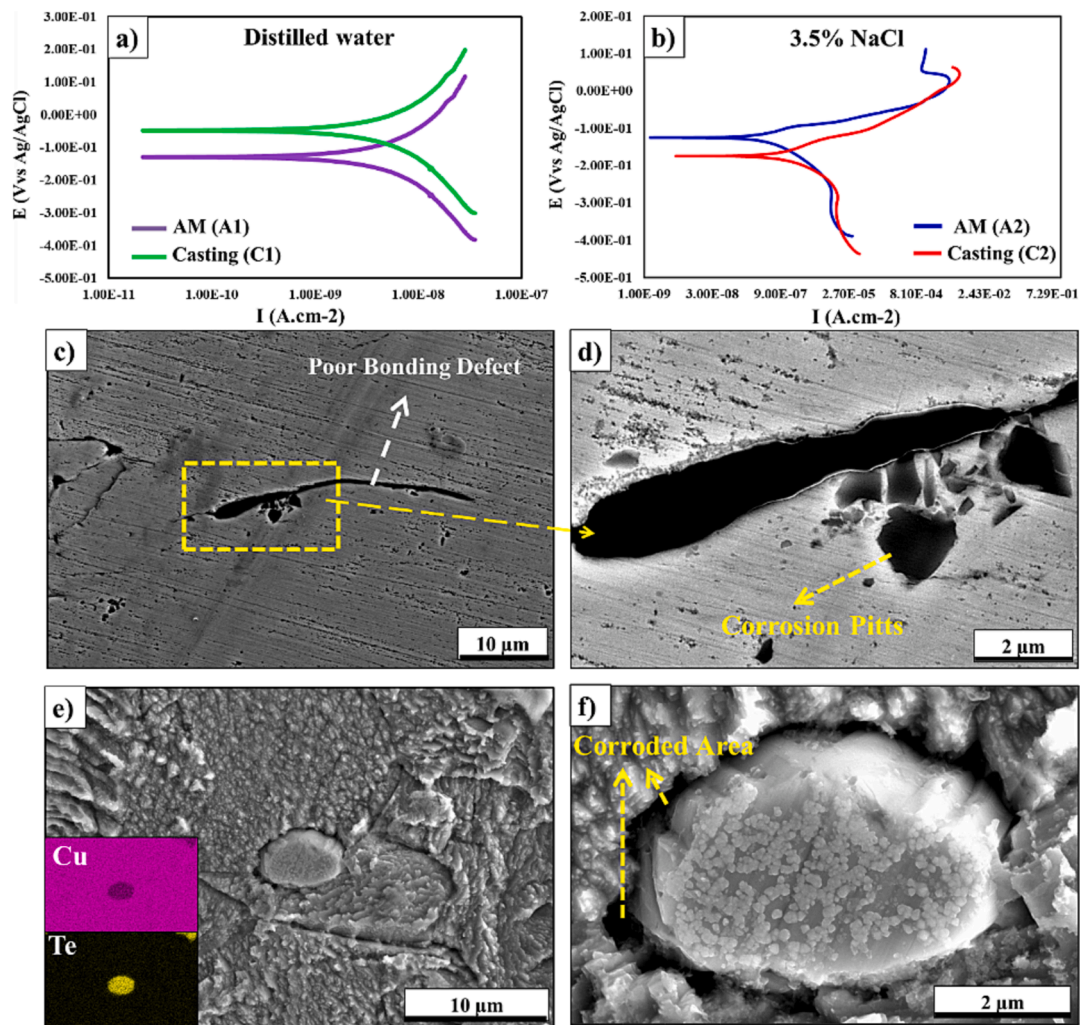
Fig. 10. Potentiodynamic polarization corrosion graphs in different environments. a) Distilled water and b) 3.5 wt% NaCl that shows more corrosion rate in the cast sample compared to the LPBF one; c) SEM image of the poor bonding defect in the LPBF sample surrounded by corrosion pits; d) High magnification corrosion pits adjacent to the defects neighborhood present in the LPBF pure copper; e) SEM image equipped along with EDS analysis of the corrosion surface of the original cast sample; f) Corroded area around the Te particles in cast pure copper.

Table 4
Corrosion parameters obtained from Tafel extrapolating to potentiodynamic polarization measurements in 3.5 wt% NaCl solution and distilled water at room temperature.

sample	I_{corr} (A/cm2)	E_{corr} (mV)	Corrosion rate (mpy)	βA (mV/decade)	βC (mV/decade)	χ^2 (chi-squared)
A1	578.0E-9	−125.0	264.0E-3	59	51	0.06×10^{-6}
C1	719.0e-9	−51.70	328.3e-3	53	55	0.0005×10^{-6}
A2	15.20e-9	−129.0	6.942e-3	66	64	0.000004×10^{-6}
C2	1.200e-6	−174.0	548.5e-3	58	61	2.3×10^{-6}

cast samples in distilled water were nearly identical. However, the corrosion potential (Ecorr) for the LPBF sample was approximately 45 mV higher than that of the cast sample, indicating that the LPBF sample is more noble in nature compared to the cast sample in NaCl solution. This observation suggests that the copper sample produced through the LPBF process is thermodynamically lower susceptible to corrosion reactions when compared to its cast counterpart in NaCl solution. It is worth noting that the kinetic aspects of the corrosion phenomenon, as indicated by the corrosion current (I_{corr}), are influenced by the microstructural features developed on the surface of the samples [72].

Although the porosities as a micrometer defect could have an important role in deteriorating the corrosion performance of the metallic components, the electrochemical behavior of the copper parts

could be more affected by the size of grains and the distribution of other alloying elements, especially Te. Fig. 10(c) and (d) show the SEM images of the corroded LPBF sample in two different magnifications. The micrographs taken from the surface of the LPBF copper component (Fig. 10 (c) and (d)) displays the presence of poor bonding areas resulting from the LOF during the LPBF process. Accordingly, the poor bonded areas as well as the pores formed during the AM process act as the micro crevice on the surface of the as-built copper part, which could localize corrosion attacks in these areas resulting in reduction of its corrosion performance.

Fig. 10(e) and (f) indicates the SEM image of the corroded cast sample in two different magnifications along with its EDS analysis. The presence of a higher amount of the Te particles in form of Cu_XTe distributed in the matrix of the cast specimen as well as their larger sizes

in comparison with those formed in the LPBF copper components, lead to inferior corrosion resistance of the cast samples than its LPBFed counterpart. Accordingly, the formation of micro galvanic cells could be promoted by higher distributions of larger Te particles in the copper matrix of the as-cast sample compared to those of the LPBF specimen [73,74]. Consequently, higher galvanic currents resulted in higher corrosion currents indicating a low corrosion performance. It was revealed using electron microscopy techniques that the Te particles in the cast sample were the preferential zones for corrosion attacks as shown in Fig. 10(e) and (f). Hence, various factors can influence the corrosion resistance of copper samples in corrosive environments, such as the presence of pores, microcracks, and the occurrence of inhomogeneous regions in the form of Cu$_X$Te particles. While pores were identified in the additive manufacturing (AM) samples, the detection of Cu$_X$Te particles was more pronounced in the as-cast samples, which were devoid of porosities. These findings suggest that the higher concentration of Cu$_X$Te particles in the as-cast samples, free from pores compared to their AM counterparts with pores, could exert a more detrimental impact on the corrosion resistance of copper samples.

A reduction in grain size could affect the corrosion resistance of the parts. Birbilis and Ralston [75] reported that grain refinement could decrease the localized corrosion rate in AM samples due to an increase in the grain boundaries as they act as the diffusion paths for the alloying elements to produce the protective layers on the surface of the alloy. Therefore, the lower grain size in the AM parts could increase their abilities to form passive layers, which increases their corrosion performance as compared to their cast counterparts.

4. Remarks on LPBF pure copper electrodes

4.1. Current status

The growing recognition among researchers and practitioners on the importance of utilizing innovative technologies to manufacture high-quality parts for various industries is evident. The priority for many industries, including aerospace, is to use complex parts that possess desirable properties, are lightweight, and have low production costs. NASA's research findings indicate that using the AM technology in the rockets can improve performance, reliability, and reduce costs compared to conventional manufacturing methods [76]. In the heat transfer industry, Saltzman et al. [77] observed a 15 % increase in efficiency after replacing the traditionally produced part with an AM part, which had different designs and properties. Precise and flawless identification of cast parts is an initial requirement for replacing parts produced by traditional methods with new techniques, such as AM.

For this purpose, in this research work, a comprehensive identification process was employed on a cast pure copper electrode using chemical, mechanical, and corrosion testing along with advanced electron microscopy techniques including TKD-EBSD analysis for the first time. This thorough analysis provided a detailed overview of physical, mechanical, chemical, and microstructural characteristics of the cast part down to the nano scale level. Eventually, the knowledge from this comprehensive identification process facilitated the design of a similar part with desired properties through laser powder bed fusion. This innovative approach consumed significant energy and resource; however, it led to a reliable AM part that can replace the conventional counterpart after precise field testing in real environments. In addition, the process can help with the certification procedure for AM parts as an obstacle for adoption.

4.2. Recommendation

While LPBF in general can lead to the improvement of the mechanical properties of pure copper, the influence of the process parameters on other physical properties in this technology cannot be overlooked. The crucial stages of this process include precise characterization of the

original component, employing the suitable equipment, selecting optimal process parameters, and performing appropriate post-processing. Selecting the proper equipment and process parameters poses a major challenge in the additive manufacturing of pure copper components, primarily due to the material's high reflectivity. The choice of laser type and shape can be particularly effective in this regard, as altering the wavelength and input energy can adjust the melting and solidification conditions.

In this work, by carefully selecting the appropriate power, speed, and laser settings, a practical pure copper sample with a density exceeding 98.5 % was successfully fabricated using LPBF. However, it was found that with a change in the height of the sample produced at a constant thickness, the percentage of porosity and subsequently the microstructure changes. In fact, the thermal history experienced by the part at different heights is the major cause of this phenomenon. Therefore, similar to Macías et al. [78] observations, by increasing the plate temperature from 35 to 200 °C, the growth rate of pores can be reduced and a different microstructure can be achieved. Therefore, the porosity in the microstructure can be reduced and the non-uniformity of the microstructure around them can be significantly improved.

As a recommendation for the issue of inhomogeneities observed through the height, a major improvement to the microstructure of the LPBF pure copper and its physical properties can be achieved using newly developed LPBF machines with heated platforms (up to 550 °C). This issue was detected in this work around finer grains closer to the pores. Fig. 11(a) shows a large IPF EBSD map of the typical LPBF pure copper, where finer grain growth around defects can be observed in Fig. 11(b). The crushing of the grains around the porosities due to the intense heat transfer into the pores and the high cooling rates are the main cause of the phenomenon seen here. This change of size and distribution of grains around the porosities can be observed almost around all pores in the microstructure (Fig. 11(c,d)). The average grain size for the overall microstructure is 12.89 μm versus 6.95 μm around the pores. Therefore, according to the results of this research and similar to the report by Pedrazzini et al. [79], it is expected that an optimal microstructure can be achieved by increasing the temperature of the build plate and controlling the thermal history.

5. Conclusions

In this study, the aim was to additively manufacture a pure copper electrode that is commonly used in electrical discharge machining equipment through the LPBF technique. Despite the challenges involved in producing a piece of pure copper with a specific geometry, the printed sample was successful in terms of its physical and dimensional aspects compared to the original cast counterpart. The microstructural features, texture, mechanical properties, and electrical and thermal conductivity coefficients along with corrosion resistance of LPBF and cast samples were investigated and compared. The conclusions of this investigation are as follows:

- The microstructure analysis of the cast sample revealed that the distribution of twins within the copper matrix was resulted from thermomechanical operations. Moreover, Te precipitates were observed with dimensions greater than 2 μm in the microstructure. Te was used to improve machining characteristics, mechanical properties, and electrical conductivity of the cast pure copper electrode.
- The microstructure of the LPBF sample exhibited variations in grain size and porosity levels across different regions of the component. Specifically, there was a notable discrepancy in porosity percentage between the thicker and thinner sections of the component close to approximately 7 %.
- Remarkably, the porosity volume of the upper part of the LPBF sample has decreased from approximately 9 % to less than 2.5 % along the direction of the building.
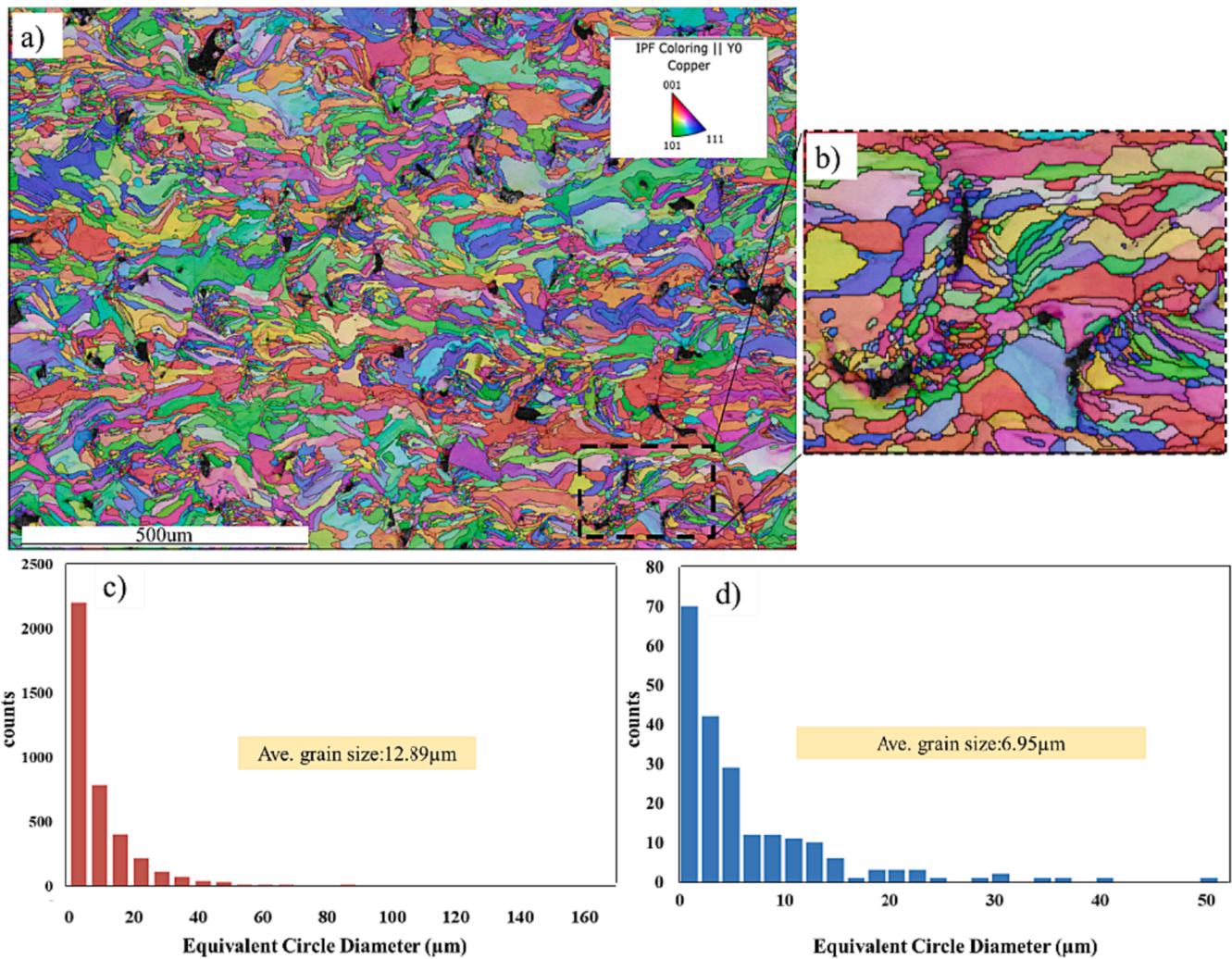
Fig. 11. IPF image of the LPBF sample a) large map image; b) fine grains around the defects; c) grain distribution of the large microstructure; d) grain distribution of the fine grains area.

- Compared to the cast sample, the LPBF sample exhibited an increase in both tensile strength and elongation percentage by 18 % and 277 %, respectively.
- The LPBF sample exhibited electrical and thermal conductivity coefficients of 5.52 S/m and 361 W/m.k, respectively. These values represented the minimum requirement for industrial use when compared to other LPBF processed samples of this type in the literature.
- Despite the presence of significant amounts of porosity and discontinuities in the LPBF sample, it was observed that the corrosion rate in the salt environment was higher in the cast sample and experienced a value of 548.56×10^{-3} (mpy). The formation of galvanic cells around the particles containing tellurium in the cast sample had a greater effect on the corrosion rate than the presence of porosity in the LPBF sample.

CRediT authorship contribution statement

Yahya Aghayar: Writing – original draft. **Parisa Moazzen:** Writing – review & editing. **Behrang Behboodi:** Methodology. **Ayda Shahriari:** Writing – review & editing. **Sajad Shakerin:** Writing – review & editing. **Alan Lloyd:** Software, Methodology. **Mohsen Mohammadi:** Writing – review & editing, Supervision.

Declaration of competing interest

The authors declare that they have no known competing financial interests or personal relationships that could have appeared to influence the work reported in this paper.

Data availability

Data will be made available on request.

Acknowledgments

References

[1] S. Qu, et al., High-precision laser powder bed fusion processing of pure copper, Addit. Manuf. 48 (2021) 102417.
[2] T. Romano, M. Vedani, Additive Manufacturing of Pure Copper: Technologies and Applications. Copper-from the Mineral to the Final Application, IntechOpen, 2022.
[3] R.N. Gu, et al., Intentional oxidation and laser remelting of highly reflective pure cu for its high-quality additive manufacturing, Adv. Eng. Mater. (2021) 2101138.

[4] P.S. Deshmukh, et al., Optimum strength and ductility of pure copper fabricated by Wire Arc Additive Manufacturing, Manufacturi. Lett. 33 (2022) 24–28.

[5] D. Ding, et al., Wire-feed additive manufacturing of metal components: technologies, developments and future interests, Int. J. Adv. Manuf. Technol. 81 (2015) 465–481.

[6] X. Song, et al., Advances in additive manufacturing process simulation: Residual stresses and distortion predictions in complex metallic components, Mater. Des. 193 (2020) 108779.

[7] V. Madhavadas, et al., A review on metal additive manufacturing for intricately shaped aerospace components, CIRP J. Manuf. Sci. Technol. 39 (2022) 18–36.

[8] R. Henderson, K. Schulmeister, Laser safety, CRC Press, 2003.

[9] W. Zouhri, et al., Characterization of laser powder bed fusion (L-PBF) process quality: a novel approach based on statistical features extraction and support vector machine, Procedia CIRP 99 (2021) 319–324.

[10] M.L. Köhler, et al., Microstructure analysis of novel LPBF-processed duplex stainless steels correlated to their mechanical and corrosion properties, Mater. Sci. Eng. A 801 (2021) 140432.

[11] Cao, S., et al., Review of laser powder bed fusion (LPBF) fabricated Ti-6Al-4V: Process, post-process treatment, microstructure, and property. Light: Advanced Manufacturing, 2021. **2**(3): pp. 313–332.

[12] Y. Chen, et al., Microstructure characterization and mechanical properties of crack-free Al-Cu-Mg-Y alloy fabricated by laser powder bed fusion, Addit. Manuf. 58 (2022) 103006.

[13] T. Ron, et al., Synthesis of refractory high-entropy alloy WTaMoNbV by powder bed fusion process using mixed elemental alloying powder, Materials 15 (12) (2022) 4043.

[14] Q. Jiang, et al., A review on additive manufacturing of pure copper, Coatings 11 (6) (2021) 740.

[15] H. von Lintel, et al., Copper alloys for additive manufacturing: Laser powder bed fusion of CuCr1Zr by using a green qcw-laser, Eur. J. Mater. (2022) 1–17.

[16] A. Singh, et al., Processability of pure Cu by LPBF using a ns-pulsed green fiber laser, Opt. Laser Technol. 154 (2022) 108310.

[17] M. Malý, et al., Effect of high-temperature preheating on pure copper thick-walled samples processed by laser powder bed fusion, J. Manuf. Process. 73 (2022) 924–938.

[18] M. Khan, P. Dickens, Selective laser melting (SLM) of gold (Au), Rapid Prototyp. J. 18 (1) (2012) 81–94.

[19] S.D. Jadhav, et al., Influence of selective laser melting process parameters on texture evolution in pure copper, J. Mater. Process. Technol. 270 (2019) 47–58.

[20] Stepien, L., et al., *Pure copper: Advanced additive manufacturing*. 2022.

[21] J. Guan, et al., Insights into fabrication mechanism of pure copper thin wall components by selective infrared laser melting, Rapid Prototyp. J. 25 (8) (2019) 1388–1397.

[22] L. Quintino, et al., Welding with high power fiber lasers–A preliminary study, Mater. Des. 28 (4) (2007) 1231–1237.

[23] E. Hori, et al., Development of SLM process using 200 W blue diode laser for pure copper additive manufacturing of high density structure, J. Laser Appl. 33 (1) (2021) 012008.

[24] S. Gruber, et al., Physical and geometrical properties of additively manufactured pure copper samples using a green laser source, Materials 14 (13) (2021) 3642.

[25] K. Niwa, et al., Few-photon color imaging using energy-dispersive superconducting transition-edge sensor spectrometry, Sci. Rep. 7 (1) (2017) 1–7.

[26] L. Gargalis, et al., Determining processing behaviour of pure Cu in laser powder bed fusion using direct micro-calorimetry, J. Mater. Process. Technol. 294 (2021) 117130.

[27] X. Liu, et al., Directed energy deposition of pure copper using blue laser, J. Manuf. Process. 85 (2023) 314–322.

[28] C. Silbernagel, et al., Electrical resistivity of pure copper processed by medium-powered laser powder bed fusion additive manufacturing for use in electromagnetic applications, Addit. Manuf. 29 (2019) 100831.

[29] D. Yanagida, et al., Electrical discharge machining using copper electrode made by additive manufacturing, Procedia CIRP 95 (2020) 449–453.

[30] W.M. Tucho, et al., Investigation of effects of process parameters on microstructure and hardness of SLM manufactured SS316L, J. Alloy. Compd. 740 (2018) 910–925.

[31] L. Constantin, et al., Laser 3D printing of complex copper structures, Addit. Manuf. 35 (2020) 101268.

[32] G.F.V. Voort, ASM handbook volume 9: metallography and microstructures, ASM Int. (2004) 1058–1060.

[33] Z. Shen, et al., Enhanced strength, ductility and electrical conductivity of Cu–Te alloys via dynamic recrystallization and precipitation, Mater. Sci. Eng. A 820 (2021) 141548.

[34] Hu, F., et al., *Effect of Cr/Te Interaction on Microstructure and Properties of a Cu-Cr-Te Alloy for Interconnecting Devices in Electrical Vehicles.*

[35] Y. Zhang, et al., First principles investigation of the structure and electronic properties of Cu2Te, Comput. Mater. Sci 81 (2014) 163–169.

[36] Q. Fu, et al., Quantitative mechanisms behind the high strength and electrical conductivity of Cu-Te alloy manufactured by continuous extrusion, J. Mater. Sci. Technol. 121 (2022) 9–18.

[37] P. Dryburgh, et al., Determining the crystallographic orientation of hexagonal crystal structure materials with surface acoustic wave velocity measurements, Ultrasonics 108 (2020) 106171.

[38] C. Dunn, F. Lionetti, The effect of orientation difference on grain boundary energies, JOM 1 (1949) 125–132.

[39] S. Mahajan, et al., Formation of annealing twins in fcc crystals, Acta Mater. 45 (6) (1997) 2633–2638.

[40] S.-W. Wang, et al., Evolution of annealing twins and recrystallization texture in thin-walled copper tube during heat treatment, Acta Metall. Sin. (Engl. Lett.) 33 (2020) 1618–1626.

[41] Maurya, A.K. and A. Kumar, *Defect and Distortion in Powder Bed Fusion of Metal Additive Manufacturing Parts.* ASEAN Journal on Science and Technology for Development, 2022. **39**(2): p. 85–103-85–103.

[42] M. Zhang, et al., Fatigue and fracture behaviour of laser powder bed fusion stainless steel 316L: Influence of processing parameters, Mater. Sci. Eng. A 703 (2017) 251–261.

[43] L. Wang, et al., Mechanism of keyhole pore formation in metal additive manufacturing, Npj Comput. Mater. 8 (1) (2022) 22.

[44] Y. Chen, et al., Defect inspection technologies for additive manufacturing, Int. J. Extreme Manuf. 3 (2) (2021) 022002.

[45] B. Zhang, Y. Li, Q. Bai, Defect formation mechanisms in selective laser melting: a review, Chin. J. Mech. Eng. 30 (2017) 515–527.

[46] Kou, S., *Welding metallurgy.* New Jersey, USA, 2003. **431**(446): p. 223-225.

[47] G. Demeneghi, et al., Size effects on microstructure and mechanical properties of additively manufactured copper–chromium–niobium alloy, Mater. Sci. Eng. A 820 (2021) 141511.

[48] A.M. Roach, et al., Size-dependent stochastic tensile properties in additively manufactured 316L stainless steel, Addit. Manuf. 32 (2020) 101090.

[49] H.-J. Lee, Effects of the energy density on pores, hardness, surface roughness, and tensile characteristics of deposited ASTM 316L specimens with powder-bed fusion process, Materials 15 (19) (2022) 6672.

[50] P. Nezhadfar, N. Shamsaei, N. Phan, Enhancing ductility and fatigue strength of additively manufactured metallic materials by preheating the build platform, Fatigue Fract. Eng. Mater. Struct. 44 (1) (2021) 257–270.

[51] M.-S. Pham, et al., The role of side-branching in microstructure development in laser powder-bed fusion, Nat. Commun. 11 (1) (2020) 749.

[52] Y. Aghayar, A. Naghashzadeh, M. Atapour, An assessment of microstructure and mechanical properties of inconel 601/304 stainless steel dissimilar weld, Vacuum 184 (2021) 109970.

[53] R. Jamaati, M.R. Toroghinejad, Effect of stacking fault energy on deformation texture development of nanostructured materials produced by the ARB process, Mater. Sci. Eng. A 598 (2014) 263–276.

[54] G. Sathiaraj, M. Ahmed, P.P. Bhattacharjee, Microstructure and texture of heavily cold-rolled and annealed fcc equiatomic medium to high entropy alloys, J. Alloy. Compd. 664 (2016) 109–119.

[55] P. Moazzen, M.R. Toroghinejad, Enhancement of mechanical properties of a novel single phase Ni1. 5FeCrCu0. 5 HEA through cold rolling and subsequent annealing, Mater. Sci. Eng. A 848 (2022) 143360.

[56] B.R. Kumar, et al., Effect of texture on corrosion behavior of AISI 304L stainless steel, Mater Charact 54 (2) (2005) 141–147.

[57] M. Ghoncheh, et al., On the microstructure and solidification behavior of new generation additively manufactured Al-Cu-Mg-Ag-Ti-B alloys, Addit. Manuf. 37 (2021) 101724.

[58] S. Qu, et al., Anisotropic material properties of pure copper with fine-grained microstructure fabricated by laser powder bed fusion process, Addit. Manuf. 59 (2022) 103082.

[59] S.D. Jadhav, et al., Laser-based powder bed fusion additive manufacturing of pure copper, Addit. Manuf. 42 (2021) 101990.

[60] Mills, K., J. Davis, and J. Destefani, *Metals Handbook, Vol. 12. Fractography.* ASM International, 1987, 1987: p. 517.

[61] J. Aegerter, et al., EN ISO 6892–1: 2009 tensile testing: initial experience from the practical implementation of the new standard, Mater. Test. 53 (10) (2011) 595–603.

[62] Y. Zhong, et al., Intragranular cellular segregation network structure strengthening 316L stainless steel prepared by selective laser melting, J. Nucl. Mater. 470 (2016) 170–178.

[63] W. Chen, et al., Effect of powder feedstock on microstructure and mechanical properties of the 316L stainless steel fabricated by selective laser melting, Metals 8 (9) (2018) 729.

[64] G. Sander, et al., Exploring the possibility of a stainless steel and glass composite produced by additive manufacturing, Mater. Des. 196 (2020) 109179.

[65] S.D. Jadhav, et al., Mechanical and electrical properties of selective laser-melted parts produced from surface-oxidized copper powder, Mater. Des. Process. Commun. 2 (2) (2020) e94.

[66] X. Yan, et al., Microstructure and mechanical properties of pure copper manufactured by selective laser melting, Mater. Sci. Eng. A 789 (2020) 139615.

[67] A. Cañadilla, et al., Mechanical, electrical, and thermal characterization of pure copper parts manufactured via material extrusion additive manufacturing, Materials 15 (13) (2022) 4644.

[68] Lu, Y., et al., *Studying electrical conductivity using a 3D printed four-point probe station.* 2017, ACS Publications.

[69] H. Bishara, et al., Understanding grain boundary electrical resistivity in Cu: the effect of boundary structure, ACS Nano 15 (10) (2021) 16607–16615.

[70] Davis, J.R., *Copper and copper alloys.* 2001: ASM international.

[71] Revie, R.W., *Corrosion and corrosion control: an introduction to corrosion science and engineering.* 2008: John Wiley & Sons.

[72] Barbir, F., *PEM fuel cells: theory and practice.* 2012: Academic press.

[73] J. Chen, et al., Non-uniform film growth and micro/macro-galvanic corrosion of copper in aqueous sulphide solutions containing chloride, Corros. Sci. 114 (2017) 72–78.

[74] M. Laleh, et al., Two and three-dimensional characterisation of localised corrosion affected by lack-of-fusion pores in 316L stainless steel produced by selective laser melting, Corros. Sci. 165 (2020) 108394.

[75] Birbilis, N. and K. Ralston, *Effect of grain size on corrosion: a review.* Corrosion, 2010. **66**: p. 075005-1.

[76] P.R. Gradl, et al., Additive manufacturing of liquid rocket engine combustion devices: a summary of process developments and hot-fire testing results. In *2018 Joint Propulsion Conference*, 2018.

[77] D. Saltzman, et al., Design and evaluation of an additively manufactured aircraft heat exchanger, Appl. Therm. Eng. 138 (2018) 254–263.

[78] J.G.S. Macías, et al., Influence on microstructure, strength and ductility of build platform temperature during laser powder bed fusion of AlSi10Mg, Acta Mater. 201 (2020) 231–243.

[79] S. Pedrazzini, et al., Effect of substrate bed temperature on solute segregation and mechanical properties in Ti–6Al–4V produced by laser powder bed fusion, Metall. Mater. Trans. A (2023) 1–17.